



Mineral magnetism of dusty olivine: A credible recorder of pre-accretionary remanence

Sophie-Charlotte L. L. Lappe and Nathan S. Church

Department of Earth Sciences, University of Cambridge, Cambridge CB2 3EQ, UK

Takeshi Kasama and Alice Bastos da Silva Fanta

Center for Electron Nanoscopy, Technical University of Denmark, DK-2800 Copenhagen, Denmark

Geoff Bromiley

Department of Earth Sciences, University of Edinburgh, Edinburgh EH9 3JW, UK

Rafal E. Dunin-Borkowski

Ernst Ruska-Centre for Microscopy and Spectroscopy with Electrons, Peter Grünberg Institute, Research Centre Jülich, D-52425 Jülich, Germany

Joshua M. Feinberg

Institute for Rock Magnetism, University of Minnesota, Twin Cities, Minneapolis, Minnesota 55455, USA

Sara Russell

Natural History Museum, London SW7 5BD, UK

Richard J. Harrison

Department of Earth Sciences, University of Cambridge, Cambridge CB2 3EQ, UK (rjh40@esc.cam.ac.uk)

[1] The magnetic properties of olivine-hosted Fe-Ni particles have been studied to assess the potential of “dusty olivine” to retain a pre-accretionary remanence in chondritic meteorites. Both body-centered (bcc) and face-centered cubic (fcc) Fe-Ni phases were formed by reduction of a terrestrial olivine precursor. The presence of Ni complicates the magnetic properties during heating and cooling due to the fcc-bcc martensitic transition. First-order reversal curve (FORC) diagrams contain a central ridge with a broad coercivity distribution extending to 600 mT, attributed to non-interacting single-domain (SD) particles, and a “butterfly” structure extending to 250 mT, attributed to single-vortex (SV) states. SD and SV states were imaged directly using electron holography. The location of the SD/SV boundary is broadly consistent with theoretical predictions. A method to measure the volume of individual SD particles using electron holography is presented. Combining the volume information with constraints on coercivity, we calculate the thermal relaxation characteristics of the particles and demonstrate that the high-coercivity component of remanence would remain stable for 4.6 Ga, even at temperatures approaching the Curie temperature of pure Fe. The high coercivity of the particles, together with the chemical protection offered by the surrounding olivine, is likely to make them resistant to shock remagnetization, isothermal remagnetization and terrestrial weathering, making dusty olivine a credible recorder of pre-accretionary magnetic fields.

Components: 10,900 words, 12 figures, 3 tables.

Keywords: chondrules; dusty olivine; electron holography; first-order reversal curves; magnetic properties; transmission electron microscopy.

Index Terms: 1519 Geomagnetism and Paleomagnetism: Magnetic mineralogy and petrology; 1540 Geomagnetism and Paleomagnetism: Rock and mineral magnetism; 3662 Mineralogy and Petrology: Meteorite mineralogy and petrology (1028, 6240).

Received 25 July 2011; **Revised** 17 October 2011; **Accepted** 17 October 2011; **Published** 17 December 2011.

Lappe, S.-C. L. L., N. S. Church, T. Kasama, A. B. da Silva Fanta, G. Bromiley, R. E. Dunin-Borkowski, J. M. Feinberg, S. Russell, and R. J. Harrison (2011), Mineral magnetism of dusty olivine: A credible recorder of pre-accretionary remanence, *Geochem. Geophys. Geosyst.*, 12, Q12Z35, doi:10.1029/2011GC003811.

Theme: Magnetism From Atomic to Planetary Scales: Physical Principles and Interdisciplinary Applications in Geoscience

Guest Editors: B. Moskowitz, J. Feinberg, F. Florindo, and A. Roberts

1. Introduction

[2] Paleomagnetism of extraterrestrial materials has the potential to provide a unique record of the magnetic fields present during the early solar system [Rochette *et al.*, 2009; Weiss *et al.*, 2010a]. For example, recent work on the post-accretionary remanence of basaltic achondrites provides evidence for an active core dynamo on differentiated parent bodies [Weiss *et al.*, 2008]. Evidence of a core dynamo has also been found in the CV carbonaceous chondrite Allende, casting doubt on the common assumption that chondrite parent bodies are undifferentiated [Carpurzen *et al.*, 2011]. The question of whether some chondritic meteorites retain a record of pre-accretionary remanence, however, remains open. Pre-accretionary signals would have been recorded by individual chondrules during their formation in the solar nebula, prior to their accretion onto their meteorite parent body. Investigating the remanent magnetization of chondrules may, therefore, provide important clues to the mechanism and location of the heating event that caused melting of the chondrule precursor - one of the most important open questions in cosmochemistry. Identifying and quantifying the pre-accretionary remanent magnetization of individual chondrules is a major scientific and technological challenge. Meteorite samples record not only primary thermoremanent magnetization (TRM) but also thermochemical remanent magnetization (TCRM) due to hydrothermal alteration and/or metamorphism, shock remanent magnetization (SRM) caused by subsequent impact events, viscous remanent magnetization (VRM) due to long-term exposure to magnetic fields (e.g., the Earth's field or

that of the parent body) or induced isothermal remanent magnetization (IRM) caused by short-term exposure to magnetic fields during collection and curation. A suitable carrier for primary TRM should therefore be chemically, thermally and magnetically very stable.

[3] Dusty olivine grains within chondritic meteorites have been proposed as a suitable candidate for retaining a faithful memory of pre-accretionary magnetic fields [Uehara and Nakamura, 2006]. These high-Mg olivine grains contain metallic Fe-Ni inclusions of various sizes, which were formed by a sub-solidus reduction of the fayalitic component (Fe_2SiO_4) of the olivine [Boland and Duba, 1981]. Dusty olivines can be found in porphyritic chondrules in unequilibrated chondrites and are proposed to be relict olivine grains (remnants of previous generations of chondrules) that survived the last chondrule formation event without melting [Nagahara, 1981]. Backscattered scanning electron microscopy (SEM) images of dusty olivine grains from the Bishunpur unequilibrated ordinary chondrite (LL3.1) are shown in Figure 1. Bishunpur is widely regarded to be among the most pristine of nebular materials, preserving a relatively unaltered record of solar nebular processes [Rambaldi and Wasson, 1981].

[4] The reduction that formed the Fe-Ni inclusions is thought to be caused by the presence of organic or graphitic carbon in the chondrule precursor [Connolly *et al.*, 1994]. It requires low oxygen fugacity (below the Fe-wüstite buffer) and temperatures between 950 and 1500°C [Boland and Duba, 1981]. Pack *et al.* [2003] observed orthoerthostite as by-product of this reaction. Natural dusty

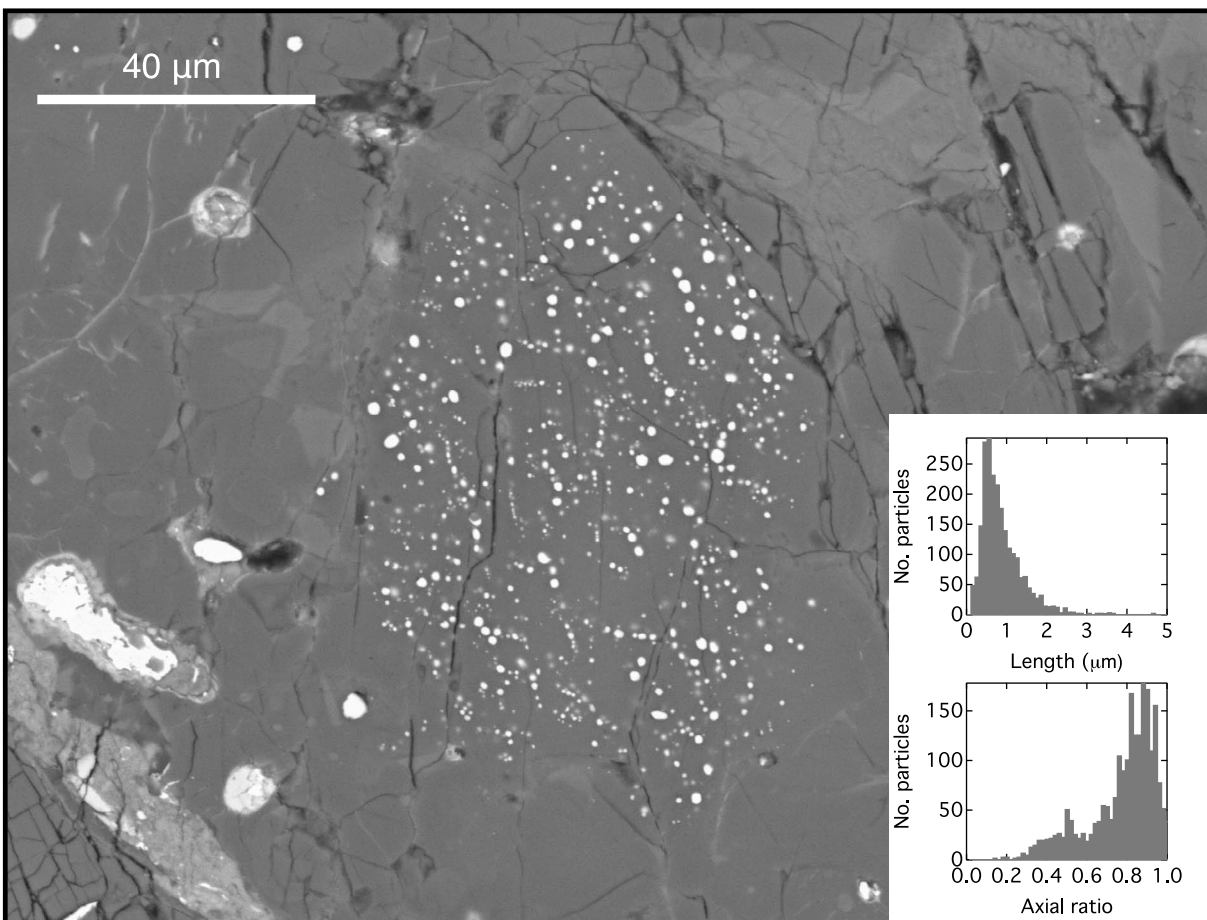


Figure 1. Backscattered SEM micrograph of a dusty olivine grain from the Bishunpur unequilibrated ordinary chondrite (LL3.1). Insets show the combined particle analyses of this and one other dusty region within the same chondrule.

olivines in chondrules exhibit various microstructural features, including a separation into dusty cores and clear rims (or vice versa) and randomly distributed bands of dusty regions within the olivine crystals [Rambaldi and Wasson, 1982; Jones and Danielson, 1997]. The size distribution of the Fe inclusions ranges from several micrometers down to a few nanometers, and inclusions are often found aligned in linear arrays [Rambaldi and Wasson, 1982; Jones and Danielson, 1997]. Electron microprobe analysis of large metal precipitates ($>5 \mu\text{m}$) show highly variable Ni-content [Rambaldi and Wasson, 1982]. Leroux *et al.* [2003] found that metal particles in the dusty olivines of the Bishunpur meteorite were single crystals with bcc structure and sometimes euhedral shapes. Occasionally they are aligned crystallographically within the host olivine, mostly exhibit low Ni-contents and are often enclosed by an amorphous glass layer. Synthetic dusty olivines displaying similar structures have been produced and described previously [Boland and Duba, 1981; Connolly *et al.*, 1994;

Leroux *et al.*, 2003; Uehara and Nakamura, 2006]. Black olivine bearing SD-SP Fe-Ni grains have also been found in two strongly shocked Martian meteorites [Van de Moortèle *et al.*, 2007].

[5] The first to consider the magnetic properties of dusty olivine were Uehara and Nakamura [2006]. Their synthetic dusty olivines showed very strong remanences with Curie temperatures of 760°C , indicating a low-Ni ($<7\text{wt}\%$) Fe-Ni alloy. Importantly, their samples proved to be exceedingly stable with respect to alternating-field (AF) demagnetization. After exposure to fields of 160 mT, samples retained between 15% and 30% of their original remanence, and the mean destructive field exceeded 80 mT. Given the highly promising magnetic characteristics established by Uehara and Nakamura [2006], further investigation of the magnetic properties of the Fe-Ni particles within dusty olivine is warranted. Here we present a mineral magnetic investigation of synthetic dusty olivine using a combination of X-ray diffraction (XRD), optical microscopy, SEM, transmission electron microscopy

Table 1. Details of Preparation Methods Used for Each Sample

Sample	Starting Material	Furnace	Heating/ Cooling Rate	Peak Temperature/ Duration	Quenching Temperature	Quenching Environment
Chond 3	Olivine/graphite	muffler	30°C/min	1350°C / 10 min	750°C	evacuated quartz tube
Chond 4	Olivine/graphite	gas-mixing	30°C/min	1350°C / 10 min	750°C	air
Chond 5	Olivine/graphite	gas-mixing	30°C/min	1315°C / 3 min	750°C	air
Chond 6	re-ground Chond 5	gas-mixing	30°C/min	1425°C / 30 min	750°C	water
Chond 7	Olivine	gas-mixing	25°C/min	1350°C / 10 min	650°C	exposed to air before quenched in water
Chond 8	Olivine	gas-mixing	25°C/min	1350°C / 10 min	650°C	exposed to air before quenched in water
Chond 9	Olivine	gas-mixing	25°C/min	1350°C / 10 min	730°C	water
Chond 10	olivine/graphite	gas-mixing	25°C/min	1350°C / 10 min	730°C	water
Chond 11	olivine/graphite	gas-mixing	25°C/min	1350°C / 10 min	1350°C	water

(TEM), temperature-dependent magnetic susceptibility (χ -T), first-order reversal curve (FORC) diagrams and off-axis electron holography (EH). Such detailed mineralogical characterization of potential remanence carriers is essential if we are to have confidence in the interpretation of paleomagnetic data obtained from meteoritic material. By direct observation of the magnetic state of individual particles, we are able to identify which are likely to be reliable remanence carriers and predict the blocking temperature as a function of observation time. The results confirm the suitability of dusty olivine as a carrier of pre-accretionary remanence and provide a useful guide for the design of a reliable paleointensity protocol. A detailed TRM study of these samples has also been carried out and will be presented in a subsequent paper focusing on a comparison of different non-heating methods of paleointensity determination.

2. Experimental Procedures

[6] Natural olivine crystals (Mg, Fe) $_2\text{SiO}_4$ from Icelandic basalt with an average composition of 10.2% fayalite and an average Ni content of 0.33 wt% oxide [MacLennan, 2008] served as starting material for the production of synthetic dusty olivines. These olivine crystals were crushed and powdered under acetone using an agate mortar, and in some experiments, pressed into a pellet. In some instances, graphite powder was added to the olivine to enhance reduction and increase the yield of Fe precipitates. The powder/pellet was then loaded into a graphite crucible, heated at a rate of 25–30°C/min to a peak temperature between 1315 and 1425°C, and held there for several minutes according to the estimated duration of a heating event associated with the formation of chondrules [Fox and Hewins, 2005]. Following this, the sample was either gradually cooled to 750°C and then quenched (in air or water), or quenched

directly from the peak temperature. To achieve the reducing conditions required for the precipitation of metallic Fe, most experiments were conducted under a pure CO-atmosphere in a gas-mixing furnace, which fixes the oxygen fugacity at the C-CO buffer [Robie *et al.*, 1979], well within the stability field of metallic Fe. One sample (chond3) was annealed in a graphite crucible within an evacuated quartz tube. Specific details of the preparation method used for each sample are given in Table 1.

[7] Samples were mounted on glass slides and polished using 3 μm diamond paste for investigation via reflected light optical microscopy. For SEM measurements the samples were given a final polish using colloidal silica. Backscattered SEM measurements were conducted on carbon-coated samples with a Helios EBS3 field-emission gun SEM using an accelerating voltage of 5–20 kV and a working distance between 3.2 and 5.3 mm. TEM images were obtained with a 100 kV Jeol JEM-100CX electron microscope operating in bright field mode. Samples were mounted on a Cu grid and argon ion milled to electron transparency. Powder XRD experiments were conducted using a Bruker D8 powder diffractometer with 2θ ranging from 10 to 130° and a step size of 0.02°. Cu $K\alpha_1$ radiation was used as X-ray source.

[8] The temperature dependence of magnetic susceptibility was measured using an MFK1-FA MultiFunction kappabridge (AGICO). All measurements were conducted using an AC field amplitude of 711 A/m, a frequency of 976 Hz and a temperature sweep rate of 11°C/min. Measurements below room temperature were made by cooling the sample to –192°C using liquid nitrogen and then recording the change in susceptibility on warming. High-temperature experiments up to 800°C were conducted under a flowing argon atmosphere to inhibit oxidation. Measured temperatures between

690 and 800°C were calibrated using the Néel temperature of pure Fe₂O₃ (Fe (III) oxide, 99.999%, product no. 52931-1, Sigma-Aldrich; $T_N = 690^\circ\text{C}$ [Özdemir and Dunlop, 2005]) and the Curie temperature of pure Fe (high purity Fe, B.C.S. No. 260/2, British Chemical Standards; $T_c = 770^\circ\text{C}$ [Ridley and Stuart, 1968]).

[9] FORC measurements [Pike *et al.*, 1999; Roberts *et al.*, 2000] were conducted on a Princeton Measurements vibrating sample magnetometer (VSM) under ambient conditions. The applied saturation field was 1.2 T. A total of 110 curves per sample were measured, giving a field step width for adjacent FORCs of 11.5 mT. FORCs were processed using FORCinel [Harrison and Feinberg, 2008] applying a smoothing factor of 3.

[10] EH measurements were acquired at the Technical University of Denmark using an FEI Titan 80–300 TEM equipped with a field-emission electron source, monochromator, spherical aberration probe corrector, Lorentz lens, and an electrostatic biprism to enable the formation of holographic interference fringes across a $\sim 1\ \mu\text{m}$ wide region of interest [Harrison *et al.*, 2002; Dunin-Borkowski *et al.*, 2004a, 2004b; Feinberg *et al.*, 2006; Harrison *et al.*, 2007; Dunin-Borkowski *et al.*, 2007]. Magnetic fields were applied to the sample in situ, prior to the acquisition of each hologram. A positive vertical magnetic field (up to 2.2 T) was generated by passing a known current through the microscope's objective lens. The sample was magnetized in the vertical field by tilting the specimen stage to an angle of either $\pm 30^\circ$ using a conventional sample holder or $\pm 78^\circ$ using a specially adapted high-tilt holder. After magnetizing, the field was switched off and the sample stage rotated back to horizontal. All holograms were acquired at remanence. The residual magnetic field at the sample due to stray fields of the electromagnetic lenses was $< 0.1\ \text{mT}$.

[11] The magnetic contribution to the total electron phase shift was isolated from the mean inner potential contribution using the reversed saturated pairs method [Dunin-Borkowski *et al.*, 2007]. A reversed saturated pair consists of two holograms obtained after tilting the specimen stage to positive and negative angles in a 2.2 T vertical field. The mean inner potential and magnetic contributions to the phase shift are determined by calculating half the sum and half the difference, respectively, of the positive-tilt and negative-tilt phase maps. This method assumes that the magnetization of the sample reverses exactly for positive and negative tilts.

Any particle that does not reverse will contribute equally to the positive-tilt and negative-tilt phase maps and its magnetic contribution is canceled out during subtraction. A higher percentage of reversed particles was found for tilt angles of $\pm 78^\circ$. To increase the number of observed particles, we used the mean inner potential map derived from the high-tilt measurements to determine the magnetic contribution in the low-tilt measurements. This procedure allowed us to observe the true magnetic signal of any particle that reversed in the $\pm 78^\circ$ tilt measurement and twice the magnetic signal of any particle that did not reverse in the $\pm 78^\circ$ measurements but did reverse in the $\pm 30^\circ$ measurements.

3. Results

3.1. Microscopic and Crystallographic Characterization

3.1.1. Optical Microscopy

[12] Reflected light optical microscopy (Figure 2) confirms the occurrence of numerous small metallic particles in the interior of the olivine crystals, giving them a dusty appearance. Larger metal precipitates are located between individual olivine grains. These features resemble those found in natural dusty olivines, with some crystals showing dusty rims and inclusion-free interiors, while others are transected by bands of dusty regions [Rambaldi and Wasson, 1982; Jones and Danielson, 1997]. Synthetic samples produced with excess powdered graphite occasionally displayed relict graphite grains that survived the heating process. Olivine grains are occasionally surrounded by a two-component adhesive, which was used to hold the sample together during the polishing process. Histograms of particle length and axial ratio are shown as insets in Figure 2. Particles range in size from a few hundred nanometers (the limit of optical resolution) to a few microns. Generally, the larger particles are equant. The grain size and axial ratio distributions of the synthetic samples compare favorably with those of natural samples (Figure 1).

3.1.2. SEM

[13] SEM images of chond4 are depicted in Figure 3. The microstructure comprises nanometer-scale Fe-Ni inclusions and larger metal aggregates within the host olivine crystals, again with similar features to those observed in natural dusty olivines. The largest particles visible in Figure 3a are $\sim 1\ \mu\text{m}$

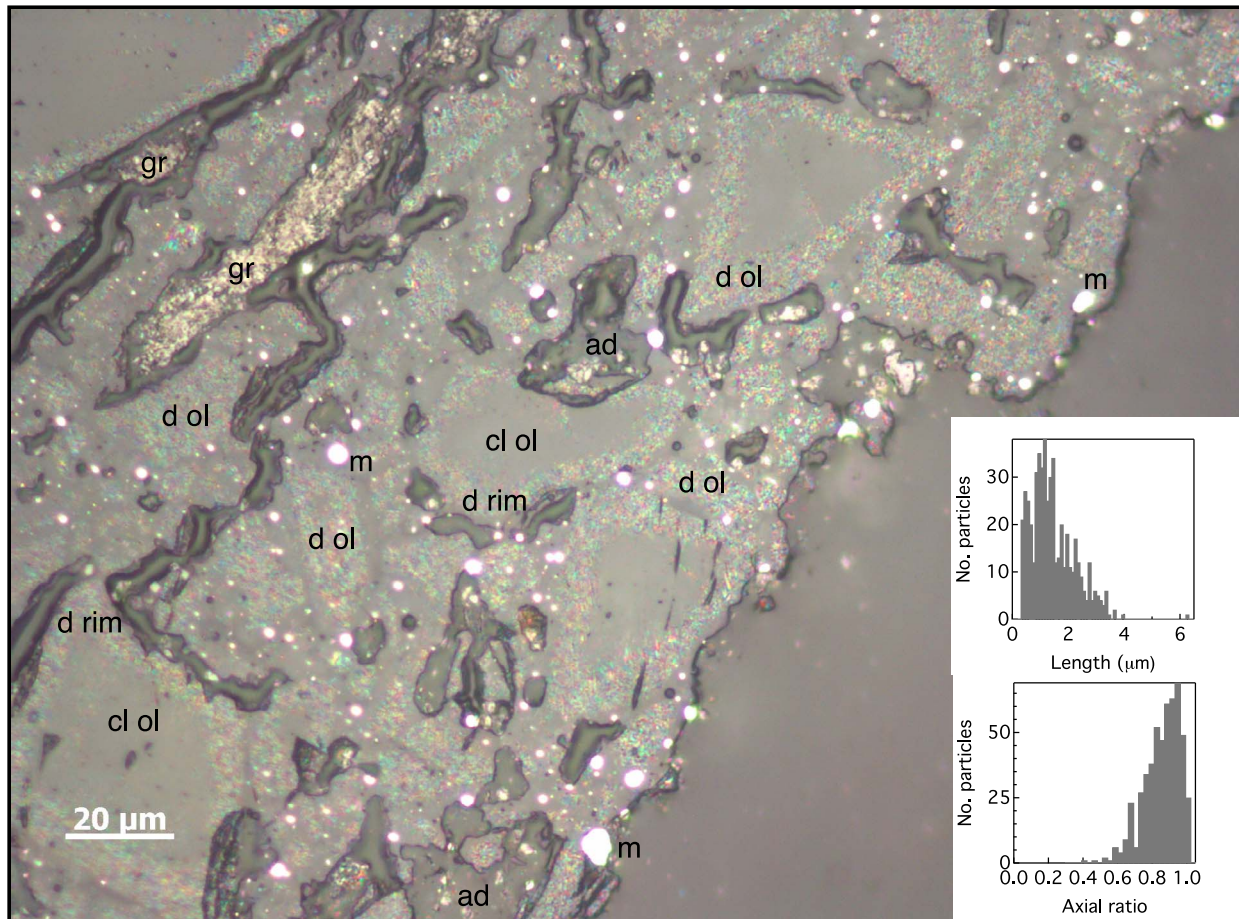
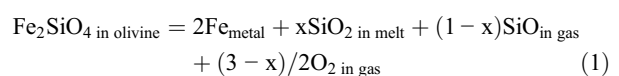


Figure 2. Reflected-light micrograph of sample chond11. d ol = dusty olivine region; d rim = dusty rim; cl ol = clear olivine; m = larger metal particles; gr = graphite; ad = adhesive. Insets show combined particle analyses of this and two other sections of the same sample.

in size. Smaller, more common, particles range in size from 10 s to 100 s of nanometers and occasionally appear to form one-dimensional chains in two distinct crystallographic orientations (Figure 3b). Figure 3c illustrates that many of these “chains” are in fact two-dimensional sheets, which appear as chains when exposed at an intersecting surface. This spatial arrangement of metal inclusions could be a result of heterogeneous nucleation on networks of dislocations or sub-grain boundaries. A higher magnification SEM image of the sample (Figure 3d) shows a range of small metal precipitates exhibiting sizes from about 300 nm down to below 100 nm. The results of particle analysis of this image are shown in Figures 3e and 3f. The observed axial ratios are again similar to those recorded for Fe particles in dusty olivines of the Bishunpur meteorite (cf. Figure 1). However, the size range examined here is about a factor of 10 smaller than in the natural sample.

3.1.3. TEM

[14] Bright field TEM images of sample chond9 (Figure 4) reveal abundant submicron-sized Fe inclusions not visible in the SEM. Their sizes range from a few hundred down to a few tens of nanometers or even smaller, some of them clearly being below the critical single-domain size for equidimensional Fe (23–28 nm [Kneller and Luborsky, 1963; Butler and Banerjee, 1975; Snoeck *et al.*, 2008]). Some of these metal particles show bubble-like light spots at their edges (Figure 4b), similar to the amorphous silica phase identified by Leroux *et al.* [2003] in association with metal inclusions in natural as well as synthetic dusty olivines. Leroux *et al.* [2003] proposed the following reduction reaction for the formation of dusty olivine:



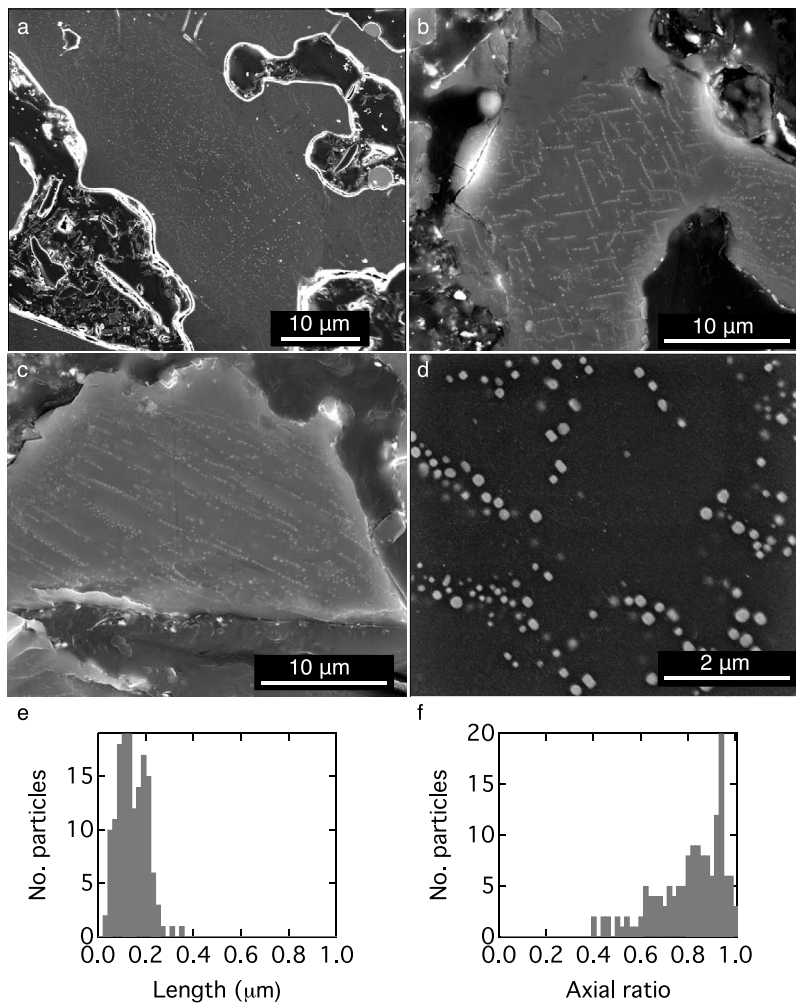
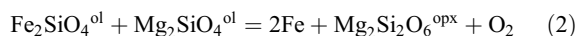


Figure 3. Backscattered SEM micrographs of sample chond4. (a) Numerous metallic inclusions in the host olivine with a few large particles of up to 1 μm in size. (b) Linear chains of metal particles forming along two crystallographically controlled directions. (c) Features resembling a sheet like arrangement of particles, probably the result of heterogeneous nucleation on dislocations or sub-grain boundaries. (d) High-magnification SEM image and corresponding particle analysis (e–f) revealing the presence of sub-100 nm particles with axial ratios as low as 0.4.

The volatilization of SiO was proposed to explain the lower-than-expected proportions of amorphous SiO₂ in relation to the amount of metallic Fe in the dusty olivine. A more likely explanation, given the comparatively low temperatures of our synthesis experiments, is that any SiO₂ released through equation (1) is unstable in the presence of forsterite and back-reacts to produce enstatite [Pack *et al.*, 2003]:



Grains of orthoenstatite showing characteristic stacking faults are clearly visible throughout the TEM samples (Figure 4c). In some cases the metal precipitates are associated with dislocations within the host olivine (Figure 4d), consistent with the

suggestion that heterogeneous nucleation on dislocation arrays (subgrain boundaries) is responsible for the planar arrangement of particles observed in SEM. Many of the metal inclusions display complex internal microstructures (Figure 5). Dark and light contours running around the perimeter of the inclusions are interpreted as thickness fringes, showing that the particles thin toward their edges. Patterns typical of twinning were commonly observed (Figure 5). These features may be linked to the fcc-bcc martensitic transition on cooling, as discussed below.

[15] Electron diffraction was used to determine the orientation relationship between the metal precipitates and the host olivine. The {110} type planes of the bcc Fe are aligned parallel to the (100) plane

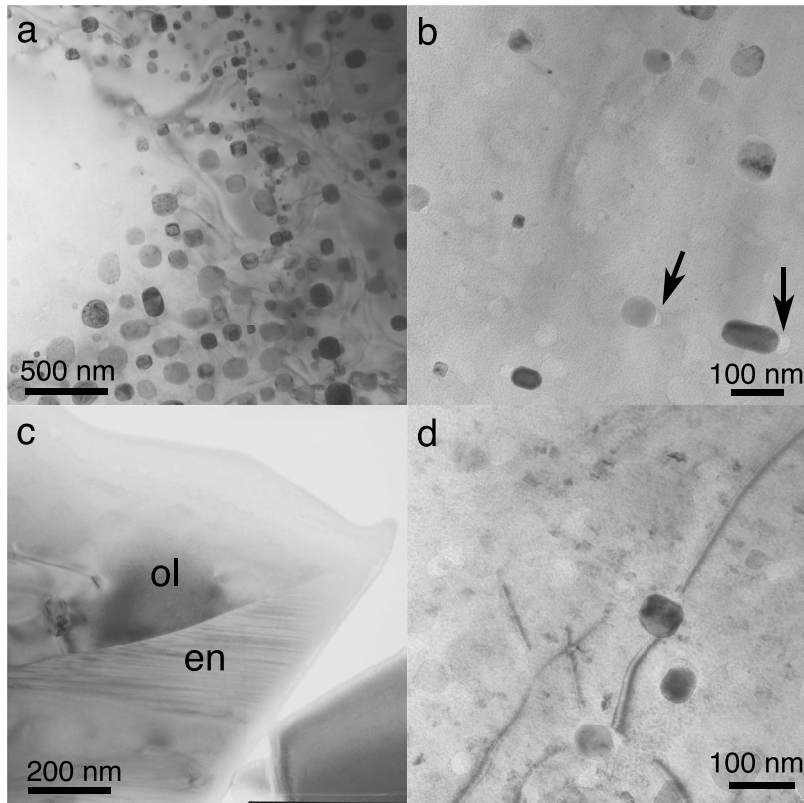


Figure 4. Bright field TEM micrographs of sample chond9. (a) Abundant Fe-Ni particles. (b) Bubble-like regions of amorphous silica (arrows) appear adjacent to many Fe-Ni particles (equation (1) [Leroux *et al.*, 2003]). (c) A grain of orthoensatite (en) with characteristic stacking faults adjacent to olivine (ol). (d) Heterogeneous nucleation of Fe particles on dislocation lines within the olivine host.

of the olivine. This same relationship was also found by Leroux *et al.* [2003]. However, the appearance of a faintly visible diffraction ring, containing all the Fe peaks, indicates that not all the inclusions are aligned perfectly within the host olivine crystal.

3.1.4. XRD

[16] Powder XRD measurements of the starting material and several reduced samples were conducted. The starting material shows forsteritic olivine as the only phase (Table 2). Using the regression equation for the forsterite-fayalite series by Schwab and Kustner [1977] the mole fraction of fayalite could be determined as $X_{Fa} = 0.13$. The reduced olivine has a lower fayalite content compared to the starting material (Table 2). The lattice parameters of chond11 yielded a negative mole fraction of fayalite, presumably indicating a composition close to pure forsterite. All reduced samples produced metallic Fe-Ni in varying amounts and structure. The bcc (kamacite) and fcc (taenite) structures are easily distinguished in XRD by the appearance of characteristic peaks at ~ 45 and ~ 43 $^{\circ}2\theta$,

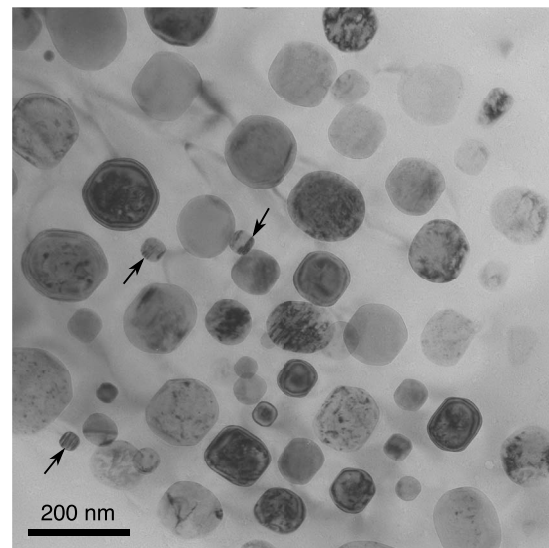


Figure 5. Bright field TEM micrograph of sample chond9 highlighting the internal microstructure observed in many particles. Dark and light contours running around the perimeter of the particles are thickness fringes. Patterns typical of twinning (arrows) are related to the fcc-bcc martensitic transition.

Table 2. Summary of XRD Data Obtained for the Starting Olivine Material and Samples Chond9, Chond10 and Chond11

	a [Å]	b [Å]	c [Å]	V [Å ³]	d ₁₃₀ [Å]	X _{Fa} ^a	Additional Phases
Starting material	4.76458(12)	10.23441(28)	5.99838(15)	292.497(13)	2.774	0.130	-
Chond 9	4.75948(32)	10.2247(7)	5.9918(4)	291.585(34)	2.771	0.085	γ-iron, α-iron, enstatite
Chond 10	4.75793(16)	10.22300(28)	5.99330(18)	291.516(15)	2.770	0.070	γ-iron, α-iron, enstatite, graphite
Chond 11	4.7448(6)	10.1783(9)	5.9720(6)	288.42(5)	2.760	<0	α-iron, enstatite, graphite

^aMole fraction fayalite according to regression equation of Schwab and Kustner [1977].

respectively. Contrary to previous studies of synthetic and natural dusty olivine, which suggest that Fe is always present in its bcc form, our results indicate that almost any combination of bcc and fcc phases can be obtained when the initial Ni content of the olivine is significant. Sample chond9 shows a high proportion of fcc Fe-Ni and only minor traces of bcc Fe. Chond10 has a much higher proportion of bcc Fe, although an fcc peak is still clearly observable. Chond11 contains a large amount of Fe solely of bcc structure. All reduced samples show additional peaks at $\sim 28^\circ 2\theta$, corresponding to the 420 peak of orthoenstatite, which is consistent with the results of previous studies [Boland and Duba, 1981; Pack et al., 2003]. Samples chond10 and chond11 also revealed the presence of a graphite phase, consistent with optical microscopy observations that some grains of the added graphite powder survived the furnace treatment. Representative XRD patterns are presented in the auxiliary material.¹

3.2. Magnetic Characterization

3.2.1. Magnetic Susceptibility Measurements

[17] Low-temperature magnetic susceptibility measurements were used to check for the presence of magnetite in freshly synthesized samples. Samples exposed to air during quenching contain significant traces of magnetite, as evidenced by the presence of a Verwey transition at -150°C . Samples quenched directly into water show no initial sign of magnetite. However, after several heating and cooling runs in an Ar atmosphere, most samples developed a clear magnetic susceptibility anomaly at $\sim -150^\circ\text{C}$, indicating that magnetite forms during the high-temperature measurements. This implies that the oxygen fugacity during a typical high-temperature susceptibility measurement lies within the stability field of magnetite (this was confirmed by measurements of a fine-grained hematite sample, which

was observed to be partially reduced to magnetite during high-temperature susceptibility measurements under flowing Ar). A high temperature susceptibility measurement of the unreduced olivine starting material showed no detectable magnetic transitions over the whole temperature range.

[18] The susceptibility curves of the first heating and cooling cycle of sample chond9 are depicted in Figure 6a. XRD indicates that this sample contains a quenched fcc Fe-Ni phase and a minor amount of bcc Fe. The quenched fcc Fe-Ni phase is paramagnetic at room temperature, which explains the sample's relatively low susceptibility at 30°C . The fcc Fe-Ni phase is metastable with respect to bcc Fe-Ni (martensite), which is itself metastable with respect to a two-phase intergrowth of bcc + fcc [Cacciamani et al., 2006]. Heating to 300°C provides sufficient thermal activation for the fcc Fe-Ni phase to undergo an isothermal martensitic transformation to ferromagnetic bcc Fe-Ni, causing a sudden increase in susceptibility at this temperature. The subsequent gradual rise in susceptibility, followed by a rapid drop at 585°C , can be assigned to the formation of magnetite during the high-temperature measurement. Between 700°C and 750°C bcc Fe-Ni transforms back to the fcc Fe-Ni phase, leading to a relatively sharp decrease in magnetic susceptibility, mirroring the increase observed at 300°C . The relatively restricted temperature range for the bcc-fcc transition on heating (starting at A_s and finishing A_f in Figure 6a) is a characteristic of the martensitic transition in Fe-Ni [Acet et al., 1995]. The loss of susceptibility at 770°C corresponds to the Curie temperature of pure bcc Fe. This loss is recovered exactly on cooling through 770°C , indicating that the pure bcc Fe particles remain chemically and thermally stable up to this temperature. The decrease in susceptibility that was observed on heating from 700 to 750°C is not recovered on cooling due to the hysteretic nature of the martensitic transition. The transition begins at a much lower temperature (labeled M_s in Figure 6a) on cooling than it does on heating, and takes place over a much broader temperature interval. The

¹Auxiliary materials are available in the HTML. doi:10.1029/2011GC003811.

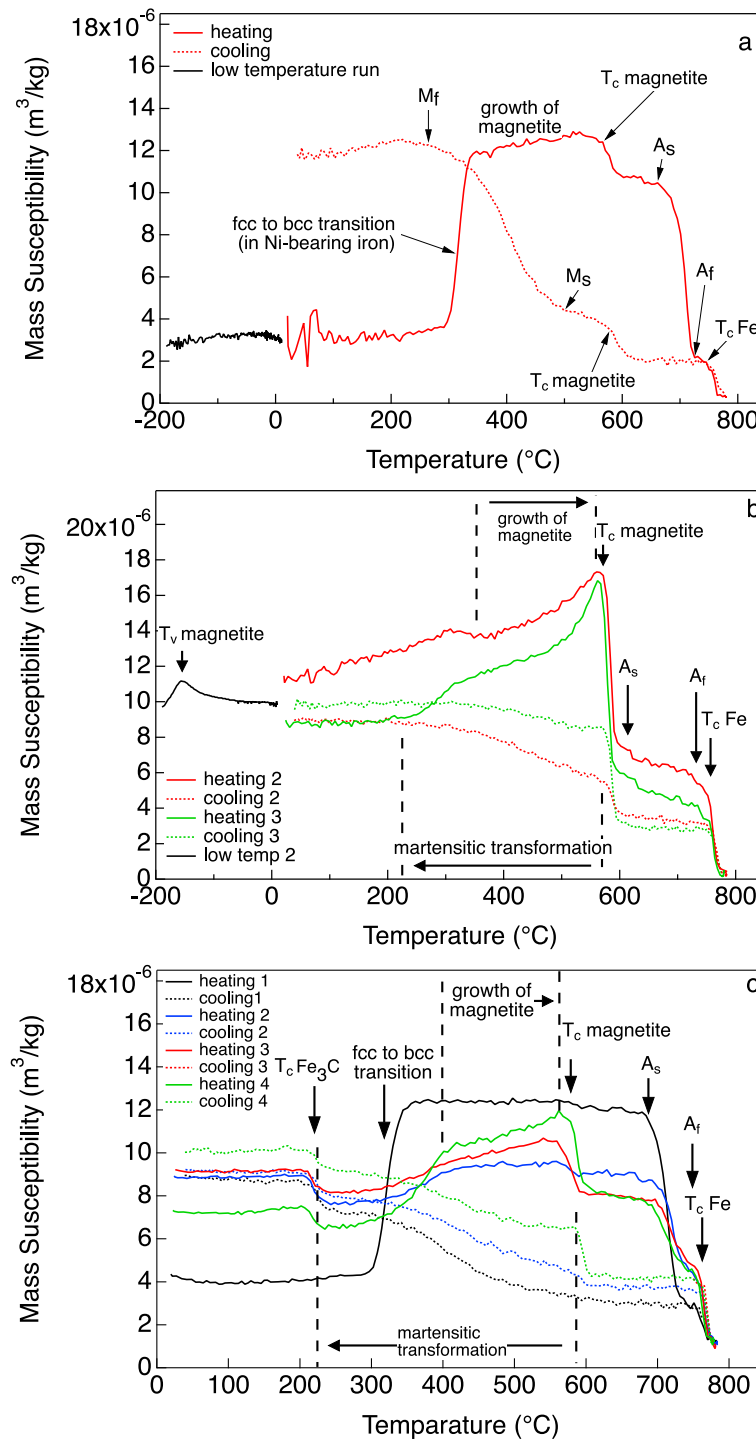


Figure 6. Mass normalized AC susceptibility versus temperature for sample chond9. (a) The first low-temperature run (black continuous line) was performed on the freshly synthesized sample. Several structural and magnetic transitions were observed in the first high-temperature heating and cooling runs (red continuous and dashed lines, respectively). A_s = austenite start temperature (i.e., the start of the bcc to fcc transition on heating), A_f = austenite finish temperature (i.e., the end of the bcc to fcc transition on heating), M_s = martensite start temperature (i.e., the start of the fcc to bcc transition on cooling), M_f = martensite finish temperature (i.e., the end of the fcc to bcc transition on cooling). (b) Second and third heating/cooling cycles for the sample from Figure 6a. The second low-temperature run (black continuous line) was performed after the third heating/cooling cycle. T_V = Verway transition. (c) Heating and cooling cycles conducted on a different piece of sample chond9. An additional anomaly at 220 $^{\circ}\text{C}$ (T_c Fe₃C) is due to a small amount of cementite.

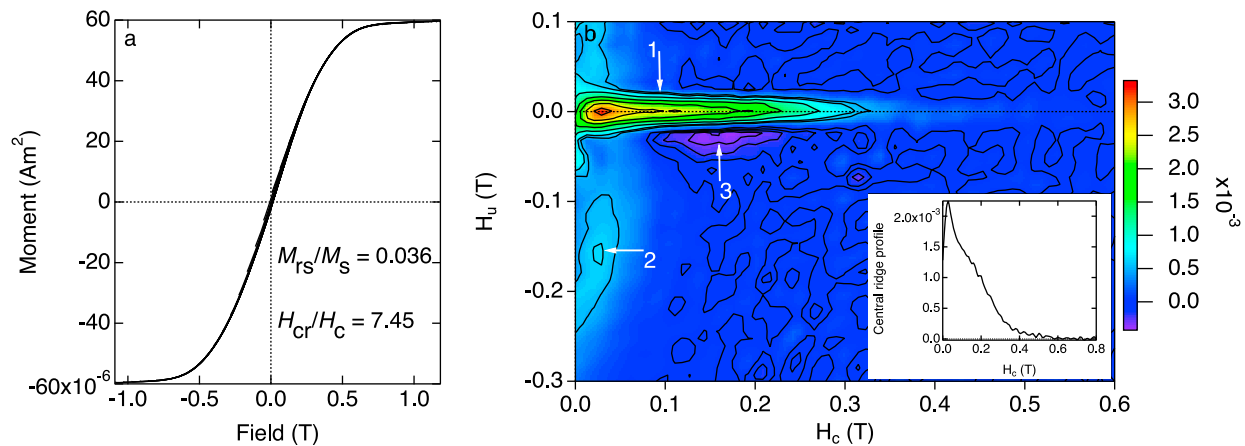


Figure 7. (a) Raw FORCs for sample chond11 (110 curves measured; every 5th curve shown). The low ratio of saturation remanent magnetization to saturation magnetization (M_{rs}/M_s) and high ratio of coercivity of remanence to coercivity (H_{cr}/H_c) would normally be considered characteristic of MD behavior [Day *et al.*, 1977]. (b) Processed FORC diagram reveals a central ridge (1), characteristic of non-interacting SD particles, and broad positive (2) and negative (3) peaks, associated with the nucleation and annihilation of SV states [Pike and Fernandez, 1999]. MD FORC signals are absent. The coercivity distribution of the central ridge (inset) extends up to ~600 mT.

cooling rate during the susceptibility measurement (11°C/min) is not high enough to quench in the fcc Fe-Ni phase. Instead a gradual increase in susceptibility is observed as fcc Fe-Ni transforms to ferromagnetic bcc Fe-Ni martensite in the temperature interval between M_s and M_f . The apparent end of the martensitic transition at M_f may, in fact, be a kinetic closure temperature, as the behavior on heating suggests that kinetics of the transformation become slower than the timescale of the experiment below 300°C.

[19] The results of two further high-temperature susceptibility measurements are depicted in Figure 6b. The heating curves show gradual growth of magnetite, the magnetite Curie temperature, the transformation from bcc to fcc Fe-Ni, and the Curie temperature of pure bcc Fe. On cooling the magnetic transitions in bcc Fe and magnetite were observed again. Typically the change in susceptibility at the magnetite Curie temperature (585°C) is smaller on cooling than it is on heating, which can be explained by the fact that magnetite is thermodynamically unstable in the presence of metallic Fe above 585°C and partly transforms to wüstite plus Fe [Presnall, 1995]. The slow rise in susceptibility below 550°C could be assigned to a gradual reformation of bcc Fe-Ni and potentially also the transformation of wüstite back to magnetite. With increasing number of heating cycles the signals attributed to fcc/bcc Fe-Ni decrease significantly, whereas those attributed to magnetite increase significantly. This suggests that Fe-Ni is being

progressively oxidized to magnetite during repeated heating. Simultaneously, the transition from bcc to fcc Fe-Ni between A_s and A_f on heating becomes less sharp, indicating that the compositional range of Fe-Ni particles is becoming wider. This may contribute to the apparent increase in the pure bcc Fe signal over time.

[20] Susceptibility measurements of a second piece of the same sample replicated all the significant features described above (Figure 6c). However, an additional anomaly was observed at around 210°C, which appeared for the first time during the first cooling cycle. The most likely explanation for this feature is the formation of small amounts of cementite (Fe_3C ; $T_c = 210^\circ C$ [Smith *et al.*, 1911]), due to reaction of Fe with the excess graphite.

3.2.2. First-Order Reversal Curve Diagrams

[21] Representative FORC data are shown in Figure 7. Despite the apparently multidomain (MD) characteristics of the individual FORC curves and extracted hysteresis parameters (Figure 7a), the presence of highly coercive particles is revealed in the processed FORC diagram (Figure 7b). The FORC distribution is dominated by a horizontal ‘central ridge’ (labeled ‘1’ in Figure 7b) with a broad coercivity (H_c) distribution that is diagnostic of non-interacting single-domain (SD) particles [Egli *et al.*, 2010]. A coercivity distribution extending from 0 to 600 mT (inset to Figure 7b) requires the presence of particles with a wide range

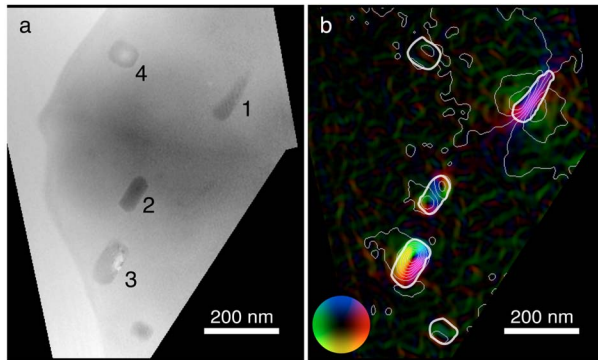


Figure 8. Electron holography results illustrating the SD and SV domain states responsible for stable remanence in dusty olivine. Reversed pairs were obtained by tilting the sample to $\pm 30^\circ$ in a 2.2 T vertical field. (a) Mean inner potential map showing particle positions. (b) Color map derived from the gradient of the magnetic contribution to the phase shift. The hue and intensity of the color indicates the direction and magnitude of the integrated in-plane component of magnetic induction, according to the color wheel (inset). Thin lines in Figure 8b are contours of the magnetic phase shift, which can be interpreted as lines of magnetic flux (the more closely spaced the contours, the higher the flux). Particle 1 shows a typical SD signal: uniform color and closely spaced contours within the particle, distinct dipolar stray fields outside the particle. Particle 2 shows a typical SV state with vortex core lying in the sample plane. Particle 3 shows a typical SV state with vortex core lying normal to the sample plane. Particle 4 appears to have no magnetic signal, which is an artifact caused by this particle's failure to reverse its magnetic state.

(~ 0.4 – 1) of axial ratios, assuming that H_c is dominated by shape anisotropy and that switching occurs via coherent rotation. The narrow vertical spread of the central ridge indicates that interparticle interaction fields (H_u) are low. Vertical spreading of the FORC distribution along the $\pm H_u$ directions is observed for $H_c < 100$ mT, indicating the presence of pseudo-single domain (PSD) and MD particles. Samples containing very large (i.e., $>10 \mu\text{m}$) particles were observed to have prominent MD signals restricted to the range $0 < H_c < 10$ mT. This MD contribution is absent in Figure 7b. Vertically spread signals in the coercivity range $10 < H_c < 100$ mT are attributed to PSD particles. The PSD signal consists of a broad positive peak (labeled ‘2’ in Figure 7b) and a broad negative peak (labeled ‘3’ in Figure 7b) just underneath the central ridge. A weak negative peak just above the central ridge was occasionally observed. The combination of positive and negative peaks can be attributed to particles in the single-vortex (SV) state [Pike and Fernandez,

1999; Dumas *et al.*, 2007a, 2007b]. The FORC coordinates of the positive peak are related to the nucleation (H_N) and annihilation (H_A) fields associated with the transition from SD to SV states and from SV to SD states, respectively [Pike and Fernandez, 1999]:

$$\{H_c, H_u\} = \{(H_A - H_N)/2, -(H_A + H_N)/2\} \quad (3)$$

Rearranging equation (3), H_N and H_A can be calculated from the FORC coordinates of the positive peak:

$$H_N = -H_c - H_u \quad (4)$$

$$H_A = H_c - H_u \quad (5)$$

Values of $H_c = 56 \pm 14$ mT and $H_u = -114 \pm 41$ mT were calculated from the average positive peak position of ~ 30 individual samples, yielding $H_N = 58 \pm 55$ mT and $H_A = 170 \pm 55$ mT. The negative peak corresponds to the lower half of a ‘butterfly’ structure that is diagnostic of SV states [Pike and Fernandez, 1999]. The butterfly is centered on FORC coordinates $\{H_c, H_u\} = \{H_A, 0\}$ and is caused by a small difference in the annihilation field for a vortex nucleating on opposite sides of a particle. The average position of the negative peak was determined to be $H_A = 183 \pm 30$ mT, which agrees well with the value of H_A determined from the position of the positive peak. This agreement confirms that both peaks are related to the nucleation and annihilation of vortices. The negative ‘annihilation’ peak extends as far as 250 mT, suggesting that AF demagnetization up to this field would be necessary to fully remove the SV contribution to remanence.

3.2.3. Electron Holography

[22] Both SD and SV states were imaged directly via EH (Figure 8). SD states were typically observed in elongated particles and were easily recognized by their distinctive external dipolar stray fields and closely spaced interior flux lines parallel to the particle length (Particle 1, Figure 8). SV states were observed in both “in-plane” and “out-of-plane” orientations, according to whether the vortex core lies in or out of the specimen plane (Particles 2 and 3, respectively, Figure 8). Electron holography is sensitive only to the in-plane component of magnetic flux. In the in-plane case we image only the central vortex core, which points roughly perpendicular to the long axis of the particle. In the out-of-plane case the central vortex core appears dark and we image the in-plane flux that circles the core.

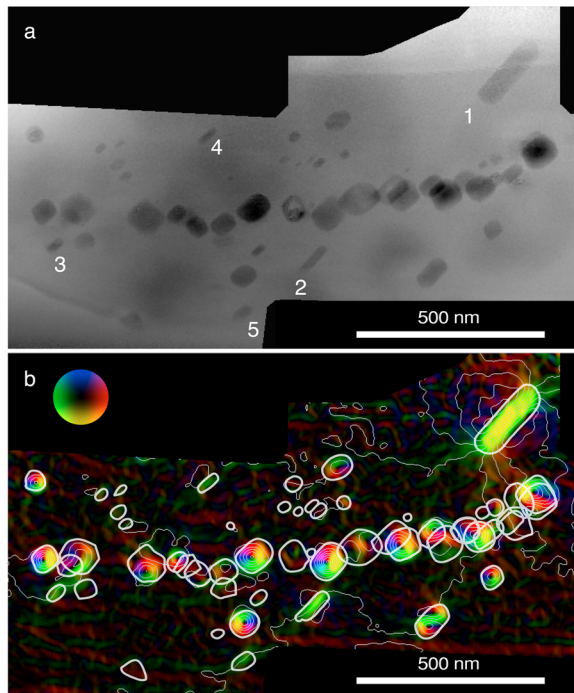


Figure 9. Electron holography results illustrating the variation in SD vs SV states for particles with a range of sizes and axial ratios. Reversed pairs were obtained by tilting the sample to $\pm 78^\circ$ in a 2.2 T vertical field. (a and b) These plots correspond to mean inner potential and magnetic flux maps, respectively, as described in the caption to Figure 8. Numbers in white refer to the SD particles analyzed and listed in Table 3.

Out-of-plane vortices were much more commonly observed than in-plane vortices. This may be a consequence of the large out-of-plane component of the saturating field applied prior to the measurement of each hologram. Alternatively it may be a consequence of the particles' dimensions in the plane of the specimen being generally larger than their thickness.

[23] Two important artifacts are visible in Figure 8. The apparent lack of magnetic signal within Particle 4 is an artifact caused by the failure of this particle to reverse its magnetization state when a saturating field was applied to the sample at $\pm 30^\circ$ tilt (no higher tilt measurements were made of this region). As described in section 2, isolating the magnetic contribution to the total electron phase shift involves subtracting pairs of phase maps obtained at positive and negative saturation [Dunin-Borkowski *et al.*, 2007]. Examination of the uncorrected phase map (Figure 8a) shows that Particle 4 has a bright center and a dark perimeter, consistent with it containing an out-of-plane vortex. Non-reversing out-of-plane

vortices were relatively common, due to the fact that magnetization reversal is achieved in these experiments by tilting the sample through $\pm 30^\circ$ while keeping the sign of the vertical saturating field constant. This geometry offers little incentive for the out-of-plane vortex core to switch sign. More success was achieved using a higher tilt angle of $\pm 78^\circ$. A phase unwrapping artifact on the right-hand-side of Particle 3 in Figure 8a leads to an artificial tightening of the phase contours in Figure 8b. Although such artifacts were rare, care was taken to reject any observation where they might adversely affect the identification of the domain state.

[24] Electron holography of a region containing over 60 particles with a range of sizes and axial ratios was performed in order to more tightly constrain the phase boundary between SD and SV states (Figure 9). Many particles are overlapping in this region (Figure 9a), although tilting of the sample demonstrated that particles were well separated in the direction of the electron beam. Of those particles that reversed their magnetization states after tilting to $\pm 78^\circ$ in a saturating field, the more elongated ones are predominantly in an SD state and the more equidimensional particles are predominantly in an out-of-plane SV state. A spectacular SD particle over 200 nm long is visible in the upper right corner. A summary of the holography results, incorporating data from all regions and applied fields studied, is presented in Figure 10 in the form of a “Butler-Banerjee” plot of domain state as a function of particle length and axial ratio [Butler and Banerjee, 1975]. Only data from non-overlapping particles with an unambiguous magnetic signal are included in Figure 10. Particle lengths and axial ratios were estimated from best fitting ellipses obtained by particle analysis of the two-dimensional mean inner potential maps (see section 2). This calculation assumes that the particles are ellipsoids of revolution. Large error bars on the axial ratios in Figure 10 indicate estimates of the uncertainty based on direct measurement of the thickness of the particles via electron holography (Table 3). Some particles were observed to switch between in-plane and out-of-plane SV states, and some were observed to switch between SV and SD states as a function of the applied field. Two phase boundaries are drawn on the plot: the lower boundary defines the limit of stable SD states; the upper boundary defines the limit of metastable SD states [Fabian *et al.*, 1996; Muxworthy and Williams, 2006]. Particles lying between the two boundaries can exist in either stable SV or metastable SD states, according to the field history of the sample. The extrapolated limit for SD

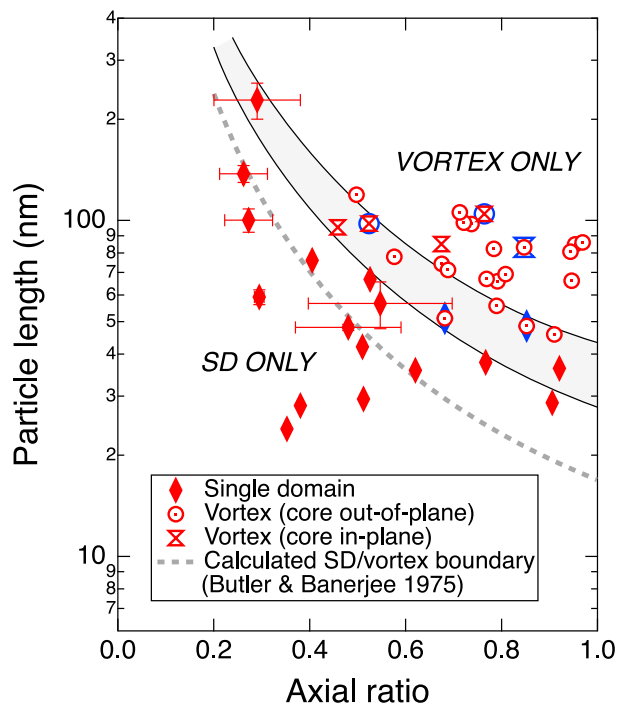


Figure 10. Phase diagram showing the limit of stability for SD states as a function of particle length and axial ratio (width/length), assuming each particle has an equidimensional cross section. Length and width were calculated from the major and minor axes of best fitting ellipses via particle analysis of the mean inner potential map (Figure 9a). Error bars are shown for the 6 SD particles listed in Table 3. These error bars illustrate the difference between the axial ratio based on particle analysis and estimates based on direct measurement of the width, length and average thickness of each particle via electron holography. SD (diamonds), out-of-plane SV (circles) and in-plane SV (hourglass) states are shown. Where a particle was observed to adopt more than one type of domain state, depending on the value of the applied field, the alternative state is shown in blue. All particles plotting to the left of the shaded area are predicted to adopt SD states. All particles plotting to the right of the shaded area (guide to eye) are predicted to adopt SV states. Particles plotting inside the shaded area are predicted to adopt either an SD or an SV state, depending on the field history. The dashed line is the theoretical limit of SD stability for prolate ellipsoidal particles [Butler and Banerjee, 1975].

states in equidimensional particles is 28 nm, which is equal to that obtained in recent micromagnetic calculations [Snoeck *et al.*, 2008]. Our results are broadly consistent with the theoretical position of the lower boundary predicted by Butler and Banerjee [1975], shown in gray.

[25] Quantitative analysis of the magnetic phase shift can, in principle, be used to determine an

Table 3. Magnetic Characteristics of SD Particles Identified by Electron Holography

Particle	Length (nm)	Width (nm)	Axial Ratio	Area (nm ²)	Moment (μ_B)	Volume (nm ³)	Average Thickness (nm)	H_c^{SW} (mT)	Contour Level ($H_c = H_c^{SW}$)	Contour Level ($H_c = 170$ mT)
1; Figure 9	200 ± 1	56 ± 1	0.2	11140	$5.46 \times 10^7 \pm 3 \times 10^4$	289112 ± 200	26 ± 1	891	7.2	6.5
2; Figure 9	92 ± 1	21 ± 1	0.22	1973	$7.40 \times 10^6 \pm 1.3 \times 10^4$	39193 ± 70	20 ± 1	869	6.3	5.6
3; Figure 9	49 ± 1	20 ± 1	0.37	930	$2.8 \times 10^6 \pm 5 \times 10^5$	14938 ± 2650	16 ± 3	683	5.8	5.2
4; Figure 9	56 ± 1	18 ± 1	0.3	1023	$2.8 \times 10^6 \pm 5 \times 10^5$	14938 ± 2650	15 ± 3	776	5.9	5.2
5; Figure 9	46 ± 1	26 ± 1	0.4	1360	$2.81 \times 10^6 \pm 5 \times 10^5$	14889 ± 2650	11 ± 3	638	5.8	5.2
1; Figure 8	146 ± 1	43 ^a ± 1	0.21	4917	$1.73 \times 10^7 \pm 1.1 \times 10^5$	91399 ± 600	19 ± 1	882	6.7	6.0

^aMeasured at its widest point.

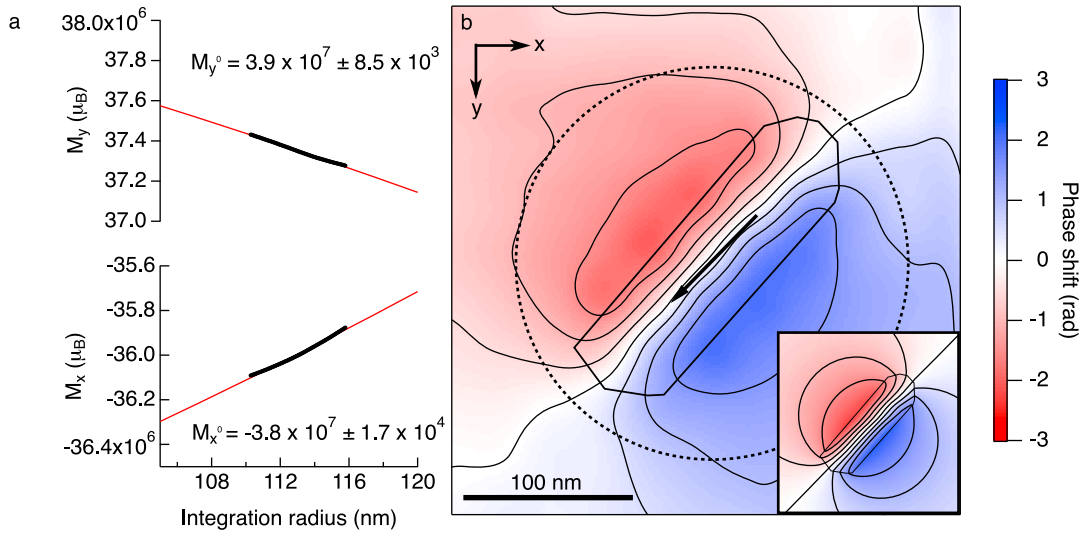


Figure 11. Example quantitative analysis of the holographic phase shift for Particle 1 from Figure 9. (a) In-plane components of magnetic moment, M_x and M_y , determined by numerical integration of equations (6) and (7) for a range of integration radii, R_c (black circles). Estimates of the true moment were determined from fits to the data using an equation of the form $M = M_0 + aR_c^2$ (red curves). (b) Contour map of the observed magnetic phase shift (radians). Dashed circle shows an integration radius of 115 nm. Black arrow shows the magnetic moment direction calculated in Figure 11a. Quantitative agreement between the simulated (inset) and observed phase shifts confirm the accuracy of the method.

absolute value for the magnetic moment of a particle. Usually, such analysis is restricted to uniformly magnetized particles with well-defined shapes (e.g., spheres), for which analytical expressions for the magnetic phase shift can be derived [Harrison *et al.*, 2007]. Recently, however, a general method for measuring the magnetic moment of a particle has been developed, that does not depend on the particle's shape or magnetization state [Beleggia *et al.*, 2010]. The measurement scheme is based on a loop integral of the phase image around a circular boundary containing the structure of interest:

$$M_x = \frac{\hbar R_c}{e\mu_0} \int_0^{2\pi} \phi(R_c \cos \theta, R_c \sin \theta) \cos \theta d\theta \quad (6)$$

$$M_y = \frac{\hbar R_c}{e\mu_0} \int_0^{2\pi} -\phi(R_c \cos \theta, R_c \sin \theta) \sin \theta d\theta \quad (7)$$

where M_x and M_y are the in-plane components of the magnetic moment vector, \hbar is the reduced Planck's constant, R_c is the radius of the integration circle, e is the electron charge, μ_0 is the permeability of free space, and $\phi(R_c \cos \theta, R_c \sin \theta)$ is the phase shift at a given angle θ around the integration circle. Values of M_x and M_y obtained by numerical integration of equations (6) and (7) around Particle 1 in Figure 9 are plotted in Figure 11a. Beleggia *et al.* [2010]

showed that the likely sources of error in this method scale with R_c^2 , and hence a measurement of the true moment (M_0) can be obtained fitting a function of the form $M = M_0 + aR_c^2$ to data obtained over a range of R_c values. Despite the limited range of usable R_c values (due to the combined effect of the particle's position at the edge of the hologram and interference from neighboring particles), a well constrained fit was obtained (Figure 11a). The resulting angle of the total moment vector agrees well with the experimental data (Figure 11b). The accuracy of the absolute value of the magnetic moment was confirmed by image simulation using the method of Beleggia and Zhu [2003], which shows excellent quantitative agreement between the measured versus predicted phase shift maps (inset to Figure 11b). Full details of these image simulations are beyond the scope of the current paper and will be presented elsewhere.

[26] Moment measurements for the five largest SD particles in Figure 9 and Particle 1 from Figure 8b are presented in Table 3, together with measurements of the lateral dimensions and cross-sectional areas determined via particle analysis. If we assume that the particles are uniformly magnetized with a saturation magnetization of 1750 kA/m [Garrick-Bethell and Weiss, 2010] then the moment measurement can be used to calculate the particle volume. The average thickness of each particle was

determined by dividing the volume by the cross-sectional area. In all cases the average thickness is less than the width of the particle. This is partly a geometrical anomaly caused by the comparison of average thickness with the full width of the particle, but also partly due to bias in the way that suitable particles are selected for study in the TEM – thinner particles produce less diffraction contrast and are less likely to produce artifacts in the phase reconstruction. Estimates of the axial ratio were determined via the formula $(\text{width} + \text{thickness})/2 * \text{length}$.

4. Discussion

4.1. Thermal Relaxation Characteristics of Potential Remanence Carriers

[27] The combination of FORC diagrams and electron holography measurements demonstrate unambiguously that remanence carriers in synthetic dusty olivine are dominated by non-interacting SD and SV states with high coercivities (up to 250 mT for SV states and up to 600 mT for SD states). Non-interacting SD particles with uniaxial shape anisotropy make ideal remanence carriers, as they obey well-established theories that allow their behavior to be predicted as a function of time, temperature and applied field [Stoner and Wohlfarth, 1948; Néel, 1949, 1955]. The direct measurement of particle volumes via electron holography allows us to place strict constraints on the thermal relaxation characteristics of the SD remanence carriers and address the critical question of whether any of the particles studied have the necessary characteristics to acquire and maintain a faithful record of pre-accretionary magnetic fields.

[28] The thermal relaxation characteristics of SD kamacite particles with uniaxial shape anisotropy can be calculated following the work by Garrick-Bethell and Weiss [2010] (which is itself based on the thermal relaxation theory of Néel [1949] and the approach of Pullaiah *et al.* [1975]). The blocking temperature, T_B , is related to the particle volume, V , saturation magnetization, $M_s(T)$, microcoercivity, $H_K(T)$ (in Tesla), and the observation time, t_{obs} , via:

$$t_{\text{obs}} = \tau_0 \exp\left(\frac{VM_s(T)H_K(T)}{2k_B T_B}\right) \quad (8)$$

where $\tau_0 = 1 \times 10^{-10}$ s, k_B is the Boltzmann constant and T is temperature. For particles dominated by shape anisotropy, the coercivity is proportional to the saturation magnetization. Hence the temperature

dependence of H_K can be expressed in terms of the temperature dependence of M_s :

$$H_K(T) = \beta(T)H_K(0) \quad (9)$$

where $\beta(T)$ is an empirical function describing the magnetic transition in Fe:

$$\beta(T) = \frac{M_s(T)}{M_s(0)} = \left(1 - 0.35(T/T_c)^{3/2} - 0.65(T/T_c)^4\right)^{1/3} \quad (10)$$

Values of $M_s(0) = 1750$ kA/m and $T_c = 1044$ K were taken from Garrick-Bethell and Weiss [2010]. Substituting equations (9) and (10) into equation (8) and rearranging we obtain the relation:

$$\frac{T_B \ln\left(\frac{t_{\text{obs}}}{\tau_0}\right)}{\beta^2(T_B)} = \frac{VM_s(0)H_K(0)}{2k_B} \quad (11)$$

The term on the left hand side of equation (11) is a two-dimensional function of T_B and t_{obs} . A contour plot of this function is shown in Figure 12. The locus of T_B as function of t_{obs} for particles with a given combination of volume and coercivity traces out a “blocking contour” on this diagram, with the contour level given by the value on the right hand side of equation (11).

[29] To calculate the correct contour level for the SD particles observed by EH (Table 3) we require an estimate of coercivity for each. With one exception, we were unable to get the SD particles to switch their magnetic state at intermediate fields (100 mT – 1.5 T) in the $\pm 30^\circ$ tilt holography measurements. The one particle that switched (particle 5 in Figure 9) did so in a field of 300 mT applied at 60° to the easy axis, which yields an intrinsic coercivity of ~ 600 mT (the intrinsic coercivity being that which would be obtained for fields applied parallel to the easy axis). This is close to the calculated coercivity of this particle based on Stoner-Wohlfarth theory and the observed average axial ratio of 0.4 ($H_c^{\text{SW}} = 638$ mT; Table 3). This agreement implies that Stoner-Wohlfarth theory provides a realistic upper estimate of coercivity for these particles. Corresponding upper limit estimates of the blocking contour levels range from 5.8 to 7.2 (Table 3), all of which place these particles on vertical blocking contours close to the Curie temperature of pure Fe (Figure 12). For particles that switch via a non-coherent rotation mechanism, the switching field will be significantly less than the Stoner-Wohlfarth values [Jacobs and Bean, 1955], especially in larger particles that might reverse by

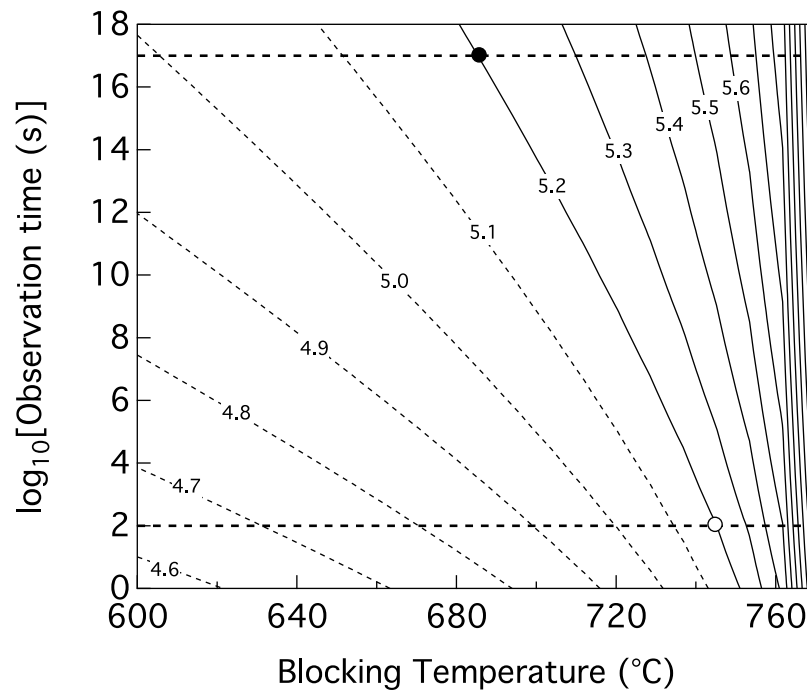


Figure 12. Blocking contour diagram for pure Fe [after Garrick-Bethell and Weiss, 2010]. Contours are labeled with a level number, x , which corresponds to a value of 10^x on the right hand side of equation (11). Contours without labels correspond to $x = 5.7$ – 6.5 in steps of 0.1. Continuous contour lines represent the predicted range of blocking behavior for the six SD particles analyzed via electron holography (Table 3). Open and closed circles represent the lower-limit blocking temperatures of Particle 5 (Figure 9) during remanence acquisition (assuming cooling occurs within 100 s) and metamorphic heating (assuming heating occurs over the whole 4.6 Ga lifetime of the meteorite), respectively. The blocking contour for Particle 1 (Figure 9) has a lower limit of $x = 6.5$ (Table 3) and would acquire a stable remanence immediately on cooling below T_c . The remanence direction would remain thermally stable at all temperatures up to T_c .

the formation and propagation of vortex states. Lower limit estimates of the blocking contour levels were calculated using a value of 170 mT for the lower limit of coercivity (this value corresponds to the lowest coercivity of SD particles that would still carry remanence after AF demagnetization to 170 mT was performed in order to remove SV remanence). Even this conservative lower estimate of coercivity leads to blocking contour levels in the range 5.2–6.5 (solid lines in Figure 12), implying that particles would acquire TRM on cooling to just 25°C below their Curie temperature during chondrule formation (assuming $t_{\text{obs}} = 10^2$ s), and that this TRM would remain thermally stable on a time scale of 4.6 Ga ($t_{\text{obs}} = 10^{17}$ s) at temperatures up to 680°C. Since this temperature is far above that experienced by any unequilibrated ordinary chondrite (the temperature during thermal alteration of the Bishunpur meteorite, for example, never exceeded 350°C [Rambaldi and Wasson, 1981]), we can conclude that the >170 mT fraction of SD particles exhibit all the necessary characteristics for acquiring and maintaining a record of pre-accretionary remanence.

4.2. Comparison Between Natural and Synthetic Dusty Olivine

[30] The results from the optical microscope, SEM and TEM observations show that the microstructures produced in this study resemble to a good approximation those of natural dusty olivine in chondrules. The metal inclusions are of comparable sizes and their microstructural distribution matches those of structures found in natural samples [Leroux *et al.*, 2003]. The XRD experiments confirmed the formation of enstatite as a by-product of this reduction, as proposed by Boland and Duba [1981] and Pack *et al.* [2003]. The magnetic susceptibility measurements demonstrate the formation of a pure Fe bcc phase that remains stable throughout several heating and cooling cycles. The stability of this high coercivity component with respect to high temperatures is crucial, as this constituent might provide the most reliable carrier of pre-accretionary remanent magnetization.

[31] Magnetic transitions related to the presence of Ni-bearing Fe-phase(s) are a complicating factor in

unraveling the magnetic properties of these samples. These transitions change with the number of heating and cooling runs, presumably due to diffusional redistribution of Fe and Ni atoms within the particles. The presence of a quenched paramagnetic fcc Fe-Ni phase in natural chondrules would have serious paleomagnetic implications, as even mild metamorphic heating on the meteorite parent body would be sufficient to cause the formation of ferromagnetic Fe-Ni martensite and the acquisition of an inverse transformation remanent magnetization. That said, TEM studies of natural samples containing dusty inclusions indicate Ni contents are typically <2wt% [Leroux *et al.*, 2003], and, therefore, natural samples are unlikely to encounter any of the complications observed in our more Ni-rich synthetics. We conclude that natural dusty olivine containing <2wt% Ni will have acquired a standard TRM on cooling and will remain thermally and chemically stable during laboratory heating.

5. Concluding Remarks

[32] The presence of high-coercivity, non-interacting SD particles dominated by shape anisotropy makes dusty olivine an ideal carrier of paleomagnetic signals. We have shown that many of these particles would acquire a stable TRM the instant they are cooled below the Curie temperature of Fe, and that this remanence would remain stable throughout the 4.6 Ga year lifetime of the meteorite. The fact that such particles are embedded within a protective matrix of silicate increases the likelihood that they will survive without oxidizing when exposed to Earth's atmosphere, and the high coercivities mean that they are also likely to withstand the generally low levels of shock typical of unequilibrated ordinary chondrites such as Bishunpur (shock grade S2 - very weakly shocked [Kojima *et al.*, 2003; Bezaeva *et al.*, 2010; Gattacceca *et al.*, 2010]). Hence dusty olivine cannot be ruled out as a carrier of pre-accretionary remanence on the basis of its mineral magnetic properties. Some open questions remain, however. First, given the uncertainty regarding the origin of chondrules, it is not clear what the orientational relationship between the chondrules and the magnetizing field might have been during their formation. For instance, impact-generated chondrules may have been moving and tumbling with respect to the magnetic field lines, similar to the impact spherules described by Weiss *et al.* [2010b], leading to erratic remanence directions. A stable direction may be recorded if chondrules are spinning about a single axis, however, as is observed in

cosmic spherules [Suavet *et al.*, 2011], although there will be a range of paleointensities recorded for a given magnetic field strength depending on the angle between the field and the chondrule spin axis. Our demonstration that many particles acquire magnetization instantly on cooling through the Curie temperature may mitigate some of these problems, as it increases the likelihood that chondrules record an instantaneous snapshot of the magnetizing field when cooling is rapid (estimates of chondrule cooling rates vary between 10 and 1000°C/hour [Hewins *et al.*, 2005]). Second, based on particle analysis (Figure 1) and the observed phase boundary between SD and SV states (Figure 10), a significant proportion of the remanence within natural dusty olivine is likely to be carried by particles in the SV state. Unlike SD states, the remanence blocking temperature of SV states is not the same as their remanence unblocking temperature, hence violating the law of reciprocity [Dunlop and Özdemir, 2001] – a standard requirement for absolute paleointensity determination using the Thellier-Thellier method. The SV remanence can either be treated as an unwanted contamination of the SD remanence, in which case it can be effectively removed by AF demagnetization to fields greater than the maximum SV annihilation field (~250 mT), or as a stable component of the pre-accretionary signal, which would require the development of a full theoretical model of PSD TRM for these particles [e.g., Winklhofer *et al.*, 1997]. The recognition of SV states as important remanence carriers in meteorites will provide fresh impetus for the development of such theories.

Acknowledgments

[33] This research was supported by the German Academic Exchange Service (DAAD), EPSRC, the Cambridge European Trust and Leverhulme grant F09633L.

References

- Acet, M., T. Schneider, and E. F. Wassermann (1995), Magnetic aspects of martensitic transformations in FeNi alloys, *J. Phys. IV*, 5, supplement, 105–109.
- Beleggia, M., and Y. Zhu (2003), Electron-optical phase shift of magnetic nanoparticles I. Basic concepts, *Philos. Mag.*, 83(8), 1045–1057, doi:10.1080/0141861031000066166.
- Beleggia, M., T. Kasama, and R. E. Dunin-Borkowski (2010), The quantitative measurement of magnetic moments from phase images of nanoparticles and nanostructures—I. Fundamentals, *Ultramicroscopy*, 110(5), 425–432, doi:10.1016/j.ultramic.2009.10.007.
- Bezaeva, N. S., J. Gattacceca, P. Rochette, R. A. Sadykov, and V. I. Trukhin (2010), Demagnetization of terrestrial

- and extraterrestrial rocks under hydrostatic pressure up to 1.2 GPa, *Phys. Earth Planet. Inter.*, *179*, 7–20, doi:10.1016/j.pepi.2010.01.004.
- Boland, J. N., and A. Duba (1981), Solid-state reduction of Fe in olivine—Planetary and meteoritic evolution, *Nature*, *294*, 142–144, doi:10.1038/294142a0.
- Butler, R. F., and S. K. Banerjee (1975), Single-domain grain size limits for metallic Fe, *J. Geophys. Res.*, *80*, 252–259, doi:10.1029/JB080i002p00252.
- Cacciamani, G., J. De Keyser, R. Ferro, U. E. Klotz, J. Lacaze, and P. Wollants (2006), Critical evaluation of the Fe-Ni, Fe-Ti and Fe-Ni-Ti alloy systems, *Intermetallics*, *14*, 1312–1325, doi:10.1016/j.intermet.2005.11.028.
- Carporzen, L., B. P. Weiss, L. T. Elkins-Tanton, D. L. Shuster, D. Ebel, and J. Gattacceca (2011), Magnetic evidence for a partially differentiated carbonaceous chondrite parent body, *Proc. Natl. Acad. Sci. U. S. A.*, *108*(16), 6386–6389, doi:10.1073/pnas.1017165108.
- Connolly, H. C., Jr., R. H. Hewins, R. D. Ash, B. Zanda, G. E. Lofgren, and M. Bourot-Denise (1994), Carbon and the formation of reduced chondrules, *Lett. Nat.*, *371*, 136–139, doi:10.1038/371136a0.
- Day, R., M. Fuller, and V. A. Schmidt (1977), Hysteresis properties of titanomagnetites: Grain-size and compositional dependence, *Phys. Earth Planet. Inter.*, *13*, 260–267, doi:10.1016/0031-9201(77)90108-X.
- Dumas, R. K., C.-P. Li, I. V. Roshchin, I. K. Schuller, and K. Liu (2007a), Magnetic fingerprints of sub-100 nm Fe dots, *Phys. Rev. B*, *75*, 134405, doi:10.1103/PhysRevB.75.134405.
- Dumas, R. K., K. Liu, C.-P. Li, I. V. Roshchin, and I. K. Schuller (2007b), Temperature induced single domain-vortex state transition in sub-100 nm Fe nanodots, *Appl. Phys. Lett.*, *91*, 202501, doi:10.1063/1.2807276.
- Dunin-Borkowski, R. E., M. R. McCartney, and D. J. Smith (2004a), Electron holography of nanostructured materials, in *Encyclopedia of Nanoscience and Nanotechnology*, vol. 3, *El–H*, edited by H. S. Nalwa, pp. 41–99, Am. Sci., Stevenson Ranch, Calif.
- Dunin-Borkowski, R. E., T. Kasama, A. Wei, S. L. Tripp, M. J. Hÿtch, E. Snoeck, R. J. Harrison, and A. Putnis (2004b), Off-axis electron holography of magnetic nanowires and chains, rings, and planar arrays of magnetic nanoparticles, *Microsc. Res. Tech.*, *64*, 390–402, doi:10.1002/jemt.20098.
- Dunin-Borkowski, R. E., T. Kasama, and R. J. Harrison (2007), Electron holography of nanostructured materials, in *Nanocharacterisation*, edited by A. I. Kirkland and J. L. Hutchison, pp. 138–183, R. Soc. of Chem., Cambridge, U. K., doi:10.1039/9781847557926-00138.
- Dunlop, D. J., and Ö. Özdemir (2001), Beyond Néel’s theories: Thermal demagnetization of narrow-band partial thermoremanent magnetizations, *Phys. Earth Planet. Inter.*, *126*, 43–57, doi:10.1016/S0031-9201(01)00243-6.
- Egli, R., A. P. Chen, M. Winklhofer, K. P. Kodama, and C. S. Horng (2010), Detection of noninteracting single domain particles using first-order reversal curve diagrams, *Geochem. Geophys. Geosyst.*, *11*, Q01Z11, doi:10.1029/2009GC002916.
- Fabian, K., A. Kirchner, W. Williams, F. Heider, T. Leibl, and A. Huber (1996), Three-dimensional micromagnetic calculations for magnetite using FFT, *Geophys. J. Int.*, *124*, 89–104, doi:10.1111/j.1365-246X.1996.tb06354.x.
- Feinberg, J. M., R. J. Harrison, T. Kasama, R. E. Dunin-Borkowski, G. R. Scott, and P. R. Renne (2006), Effects of internal mineral structures on the magnetic remanence of silicate-hosted titanomagnetite inclusions: An electron holography study, *J. Geophys. Res.*, *111*, B12S15, doi:10.1029/2006JB004498.
- Fox, G. E., and R. H. Hewins (2005), Chondrule reheating experiments and relict olivine, *Geochim. Cosmochim. Acta*, *69*(9), 2441–2449, doi:10.1016/j.gca.2004.11.014.
- Garrick-Bethell, I., and B. P. Weiss (2010), Kamacite blocking temperatures and applications to lunar magnetism, *Earth Planet. Sci. Lett.*, *294*(1–2), 1–7, doi:10.1016/j.epsl.2010.02.013.
- Gattacceca, J., M. Boustie, L. Hood, J. P. Cuq-Lelandais, M. Fuller, N. S. Bezaeva, T. de Resseguier, and L. Berthe (2010), Can the lunar crust be magnetized by shock: Experimental groundtruth, *Earth Planet. Sci. Lett.*, *299*, 42–53, doi:10.1016/j.epsl.2010.08.011.
- Harrison, R. J., and J. M. Feinberg (2008), FORCinel: An improved algorithm for calculating first-order reversal curve distributions using locally weighted regression smoothing, *Geochem. Geophys. Geosyst.*, *9*, Q05016, doi:10.1029/2008GC001987.
- Harrison, R. J., R. E. Dunin-Borkowski, and A. Putnis (2002), Direct imaging of nanoscale magnetic interactions in minerals, *Proc. Natl. Acad. Sci. U. S. A.*, *99*, 16,556–16,561, doi:10.1073/pnas.262514499.
- Harrison, R. J., R. E. Dunin-Borkowski, T. Kasama, E. T. Simpson, and J. M. Feinberg (2007), Properties of rocks and minerals—Magnetic properties of rocks and minerals, in *Treatise on Geophysics*, vol. 2, *Mineral Physics*, edited by G. D. Price, pp. 618–630, Elsevier, New York.
- Hewins, R. H., H. C. Connolly Jr., G. E. Lofgren, and G. Libourel (2005), Experimental constraints on chondrule formation, in *Chondrites and the Protoplanetary Disk*, edited by A. N. Krot, E. R. D. Scott, and B. Reipurth, *Astron. Soc. Pac. Conf. Ser.*, *341*, 286–316.
- Jacobs, I. S., and C. P. Bean (1955), An approach to elongated fine-particle magnets, *Phys. Rev.*, *100*, 1060–1067, doi:10.1103/PhysRev.100.1060.
- Jones, R. H., and L. R. Danielson (1997), A chondrule origin for dusty relict olivine in unequilibrated chondrites, *Meteorit. Planet. Sci.*, *32*, 753–760, doi:10.1111/j.1945-5100.1997.tb01565.x.
- Kneller, E. F., and F. E. Luborsky (1963), Particle size dependence of coercivity and remanence of single-domain particles, *J. Appl. Phys.*, *34*, 656–658, doi:10.1063/1.1729324.
- Kojima, T., D. S. Lauretta, and P. R. Buseck (2003), Accretion, dispersal, and reaccumulation of the Bishunpur (LL3.1) brecciated chondrite: Evidence from troilite-silicate-metal inclusions and chondrule rims, *Geochim. Cosmochim. Acta*, *67*(16), 3065–3078, doi:10.1016/S0016-7037(03)00025-5.
- Leroux, H., G. Libourel, L. Lemelle, and F. Guyot (2003), Experimental study and TEM characterization of dusty olivines in chondrites: Evidence for formation by in situ reduction, *Meteorit. Planet. Sci.*, *38*, 81–94, doi:10.1111/j.1945-5100.2003.tb01047.x.
- MacLennan, J. (2008), Lead isotope variability in olivine-hosted melt inclusions from Iceland, *Geochim. Cosmochim. Acta*, *72*, 4159–4176, doi:10.1016/j.gca.2008.05.034.
- Muxworthy, A. R., and W. Williams (2006), Critical single-domain/multidomain grain sizes in noninteracting and interacting elongated magnetite particles: Implications for magnetosomes, *J. Geophys. Res.*, *111*, B12S12, doi:10.1029/2006JB004588.
- Nagahara, H. (1981), Evidence for secondary origin of chondrules, *Nature*, *292*, 135–136, doi:10.1038/292135a0.

- Néel, L. (1949), Théorie du traînage magnétique des ferromagnétiques en grains fins avec applications aux terres cuites, *Ann. Geophys.*, *5*, 99–136.
- Néel, L. (1955), Some theoretical aspects of rock magnetism, *Adv. Phys.*, *4*, 191–243, doi:10.1080/00018735500101204.
- Özdemir, Ö., and D. J. Dunlop (2005), Thermoremanent magnetization of multidomain hematite, *J. Geophys. Res.*, *110*, B09104, doi:10.1029/2005JB003820.
- Pack, A., S. Hoernes, T. Walther, and R. Bross (2003), Behavior of basic refractories at high temperatures and implications for the usability of olivine as refractory material, *Eur. J. Mineral.*, *15*, 193–205, doi:10.1127/0935-1221/2003/0015-0193.
- Pike, C. R., and A. Fernandez (1999), An investigation of magnetic reversal in submicron-scale Co dots using first order reversal curve diagrams, *J. Appl. Phys.*, *85*, 6668–6675, doi:10.1063/1.370177.
- Pike, C. R., A. P. Roberts, and K. L. Verosub (1999), Characterizing interactions in fine magnetic particle systems using first order reversal curves, *J. Appl. Phys.*, *85*, 6660–6667, doi:10.1063/1.370176.
- Presnall, D. C. (1995), Phase diagrams of earth-forming minerals, in *Mineral Physics and Crystallography: A Handbook of Physical Constants*, AGU Ref. Shelf, vol. 2, edited by T. J. Ahrens, pp. 248–268, AGU, Washington, D. C., doi:10.1029/RF002p0248.
- Pullaiah, G., E. Irving, K. L. Buchan, and D. J. Dunlop (1975), Magnetization changes caused by burial and uplift, *Earth Planet. Sci. Lett.*, *28*, 133–143, doi:10.1016/0012-821X(75)90221-6.
- Rambaldi, E. R., and J. T. Wasson (1981), Metal and associated phases in Bishunpur, a highly unequilibrated ordinary chondrite, *Geochim. Cosmochim. Acta*, *45*, 1001–1015, doi:10.1016/0016-7037(81)90127-7.
- Rambaldi, E. R., and J. T. Wasson (1982), Fine, nickel-poor Fe-Ni grains in the olivine of unequilibrated ordinary chondrites, *Geochim. Cosmochim. Acta*, *46*, 929–939, doi:10.1016/0016-7037(82)90049-7.
- Ridley, N., and H. Stuart (1968), Lattice parameter anomalies at the Curie point of pure Fe, *Br. J. Appl. Phys.*, *1*, 1291–1295.
- Roberts, A. P., C. R. Pike, and K. L. Verosub (2000), First-order reversal curve diagrams: A new tool for characterizing the magnetic properties of natural samples, *J. Geophys. Res.*, *105*, 28,461–28,475, doi:10.1029/2000JB900326.
- Robie, R. A., B. S. Hemingway, and J. R. Fisher (1979), Thermodynamic properties of minerals and related substances at 298.15 K and 1 bar (10^5 Pascals) pressure and at higher temperatures, *U.S. Geol. Surv. Bull.*, *1452*, 1–456.
- Rochette, P., B. P. Weiss, and J. Gattacceca (2009), Magnetism of extraterrestrial materials, *Elements*, *5*(4), 223–228, doi:10.2113/gselements.5.4.223.
- Schwab, R. B., and D. Kustner (1977), Präzisionsgitterkonstantenbestimmung zur Festlegung röntgenographischer Bestimmungskurven für synthetische Olivine der Mischkristallreihe Forsterit-Fayalit, *Neues Jahrb. Mineral. Monatsh.*, *5*, 205–215.
- Smith, S. W. J., W. White, and S. G. Barker (1911), The magnetic transition temperature of cementite, *Proc. Phys. Soc. London*, *24*, 62–69, doi:10.1088/1478-7814/24/1/310.
- Snoeck, E., C. Gatel, L. M. Lacroix, T. Blon, S. Lachaize, J. Carrey, M. Respaud, and B. Chaudret (2008), Magnetic configurations of 30 nm iron nanocubes studied by electron holography, *Nano Lett.*, *8*(12), 4293–4298, doi:10.1021/nl801998x.
- Stoner, E. C., and E. P. Wohlfarth (1948), A mechanism of magnetic hysteresis in heterogeneous alloys, *Philos. Trans. R. Soc. A*, *240*, 599–642.
- Suavet, C., J. Gattacceca, P. Rochette, and L. Folco (2011), Constraining the terrestrial age of micrometeorites using their record of the Earth's magnetic field polarity, *Geology*, *39*(2), 123–126, doi:10.1130/G31655.1.
- Uehara, M., and N. Nakamura (2006), Experimental constraints on magnetic stability of chondrules and the paleomagnetic significance of dusty olivines, *Earth Planet. Sci. Lett.*, *250*, 292–305, doi:10.1016/j.epsl.2006.07.042.
- Van de Moortèle, B., B. Reynard, P. Rochette, M. Jackson, P. Beck, P. Gillet, P. F. McMillan, and C. A. McCammon (2007), Shock-induced metallic iron nanoparticles in olivine-rich Martian meteorites, *Earth Planet. Sci. Lett.*, *262*, 37–49, doi:10.1016/j.epsl.2007.07.002.
- Weiss, B. P., J. S. Berdahl, L. Elkins-Tanton, S. Stanley, E. A. Lima, and L. Carporzen (2008), Magnetism on the angrite parent body and the early differentiation of planetesimals, *Science*, *322*, 713–716, doi:10.1126/science.1162459.
- Weiss, B. P., J. Gattacceca, S. Stanley, P. Rochette, and U. R. Christensen (2010a), Paleomagnetic records of meteorites and early planetesimal differentiation, *Space Sci. Rev.*, *152*(1–4), 341–390, doi:10.1007/s11214-009-9580-z.
- Weiss, B. P., S. Pedersen, I. Garrick-Bethell, S. T. Stewart, K. L. Louzada, A. C. Maloof, and N. L. Swanson-Hysell (2010b), Paleomagnetism of impact spherules from Lonar crater, India and a test for impact-generated fields, *Earth Planet. Sci. Lett.*, *298*(1–2), 66–76, doi:10.1016/j.epsl.2010.07.028.
- Winklhofer, M., K. Fabian, and F. Heider (1997), Magnetic blocking temperatures of magnetite calculated with a three-dimensional micromagnetic model, *J. Geophys. Res.*, *102*, 22,695–22,709, doi:10.1029/97JB01730.